SCIENTIFIC REPORTS
nature research

OPEN

Structural, optical, thermal and conducting properties of $V_{2-x}Li_xO_{5-\delta}$ ($0.15 \leq x \leq 0.30$) systems

Savidh Khan & K. Singh*

Lithium-doped vanadates ($V_{2-x}Li_xO_{5-\delta}$ ($0.15 \leq x \leq 0.30$)) are synthesized by melt-quench method. The physical, structural, optical, thermal and conducting properties of as-quenched samples are investigated using various experimental techniques to study their suitability for electrolyte in battery/solid oxide fuel cell application. X-ray diffraction (XRD) patterns confirm the formation of three different crystalline phases. FTIR and Raman spectra indicate that the doping of Li_2O into V_2O_5 leads to a transition from VO_5 into VO_4 structural unit. The optical diffused reflectance spectra revealed that the optical band gap (E_g) decreases from 2.2 to 2.08 eV while Urbach energy (E_U) increases (0.31–0.41 eV) with the addition of Li_2O content in place of vanadium. The thermal stability is studied by thermogravimetric analyser (TGA). The DC conductivity of the present samples is increased from 0.08 to 0.12 Scm^{-1} at 450 °C with Li_2O doping. These materials can be used as electrolyte for battery/solid oxide fuel cell due to their good conductivity (~0.12 Scm^{-1}) at 450 °C.

Solid oxide fuel cells (SOFCs) are most efficient electrochemical devices which convert chemical energy into electricity with heat and water as a by-product. SOFCs are considered as eco-friendly since there is no production of sulfur or nitrogen oxides (only CO_2) along with fuel flexibility (H_2, CO, hydrocarbons and biogases)[1–3]. Since, the high operating temperature of SOFC leads to degradation, coefficient of thermal expansion mismatch, electrode sintering and catalyst poisoning among the components of SOFCs[1–3]. Thus, a lot of research is carried out to develop new materials that can meet the requirements at lower operating temperature of SOFCs[3–5]. Doped V_2O_5 materials can be a good choice for low temperature (600–800 °C) SOFCs applications due to their good conductivity at lower temperature[6]. The electrical conduction in V_2O_5 based materials arises by exchanging of unpaired $3d^1$ electrons (hopping) between V^{4+} and V^{5+} valence states, V^{4+}-O-V^{5+}-O-V^{4+}. These unpaired electrons are induced polarization around vanadium ions which leads to form polaron[6,7]. Alkali metal oxide doped vanadates have been studied widely due to their numerous applications in optical and electronic devices[1,2,8]. The chemical nature and concentration of dopants play a vital role to change the oxidation state of vanadium which leads to a creation of oxygen vacancies to maintain overall electrical neutrality of the vanadate systems[5,9,10]. Punia *et al.* have reported the increasing trend of density and molar volume due to change in structure from VO_4 tetrahedral to VO_5 trigonal bi-pyramid with the addition of Bi_2O_3 in zinc vanadates[11]. In addition to this, alkali ions doped materials usually show mixed electronic and ionic conductivity behavior with temperature. Doped bismuth vanadates ($Bi_4V_2O_{11-\delta}$) show good conductivity ~0.2 Scm^{-1} at 500 °C due to the higher oxygen vacancies and stabilization of high conducting γ-phase at room temperature[12]. The highest conductivity i.e. 6.6×10^{-4} Scm^{-1} for $Bi_4V_{2-x}Al_xO_{11-\delta}$ ($x = 0.2$) system at 500 °C has been reported by Ravikant *et al.*[4]. Chakrabarty *et al.*[13] studied the doping effect of Na_2O on conducting properties of Na_2O-V_2O_5 system and found an increment in conductivity (0.05×10^{-3}–19.5×10^{-3} Scm^{-1}) with Na_2O concentration at room temperature. A study of $V_{2-x}Mg_xO_{5-\delta}$ ($x = 0.05$–0.30) systems has been revealed a decreasing trend in density (3.2–2.7 gcm^{-3}) and thermal stability with MgO concentration. The structural transition has occurred from VO_5 to VO_4 polyhedra with MgO dopant. DC conductivity decreases from 10^{-1} Sm^{-1} to 10^{-4} Sm^{-1} while activation energy increases from 0.27 to 0.44 eV with an increase in MgO content in place of vanadium[6]. The optical bandgap increases whereas Urbach energy decreases with the increasing content of Bi_2O_3 due to decreasing oxygen vacancies[14].

School of Physics and Materials Science, Thapar Institute of Engineering & Technology, Patiala, 147004, India.
*email: kusingh@thapar.edu

Sample ID	Molecular weight, M (gmol^{-1})	Density, ρ (gcm^{-3})	Molar volume, V_m (cm^{3}mol^{-1})	Ionic concentration, N_i ($\times 10^{23}$ cm^{-3})	Inter-ionic distance, R_i (Å)	Polaron radius, r_p (Å)
VL-0.15	170.48	3.09	55.17	1.63	1.82	0.73
VL-0.20	166.68	3.00	55.56	2.16	1.66	0.67
VL-0.25	162.88	2.93	55.59	2.70	1.54	0.62
VL-0.30	159.08	2.86	55.62	3.24	1.45	0.58

Table 1. Physical parameters with their labels of the as quenched samples.

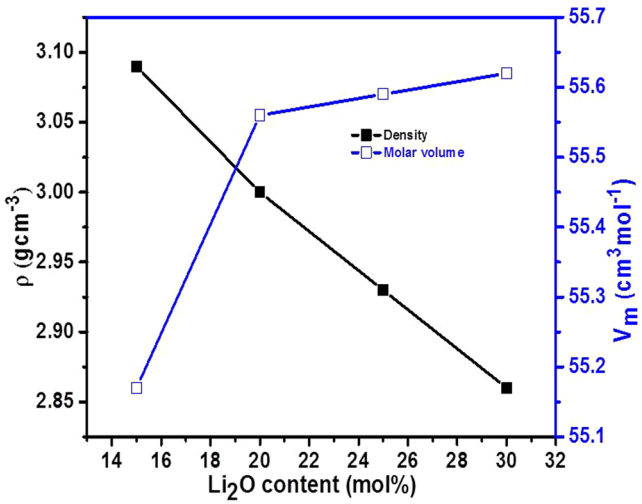

Figure 1. Change in density and molar volume with Li_2O content in V_2O_5.

Electrical properties of MnO_2 doped V_2O_5 system are also reported[15]. Tsuzuki *et al.*[16] have investigated V_2O_5-MO (M = Mg, Ca and Ba) systems and correlate the structural changes with electrical properties. In most of the cases, these doped systems are prepared by solid-state reaction/chemical method followed by slow cooling which leads to lower the conductivity due to ordering in oxygen vacancies[5]. It has been reported by some research groups that quenched samples have higher disordering/defects which leads to increase in the overall electrical conductivity. The high quenching rate encourages the reduction of vanadium which leads to higher disordering and hence may increase the overall conductivity[5,17]. Based on above discussion, it could be concluded that processing parameters and chemical nature of dopants affect the properties significantly particularly conductivity. Therefore, the motivation of the present work is to study the effect of systematic change of lower valance dopant (Li_2O) concentration on optical, thermal and conducting properties of V_2O_5 grown by melt-quench technique. The $V_{2-x}Li_xO_{5-\delta}$ ($x = 0.15$–0.30) systems have been synthesized by melt-quench followed by various characterization techniques to study their structural, optical, thermal and electrical properties to check their suitability as electrolytes for SOFCs applications.

Results and Discussion

Physical properties. Various physical parameters such as density, molar volume and ionic concentration and their inter-ionic distance and polaron radius are calculated for the as-quenched samples and depicted in Table 1.

Figure 1 shows the variation of density (ρ) and molar volume (V_m) with Li_2O dopant of as-quenched samples. It is cleared (Fig. 1) that the density decreases while molar volume increases with increasing Li_2O content. This decrement in the density is due to the replacement of the heavier V_2O_5 (3.36 gcm^{-3}) by the lighter Li_2O (2.01 gcm^{-3})[6,18]. On the other hand, the doping of Li^{1+} into V^{5+} also creates oxygen vacancies. The size of oxygen vacancy is smaller as compared to the size of the oxygen anion O^{2-}. So, the volume of the samples with dopant also decreases which leads to increase in the density. However, a lower density of dopant Li_2O as compared to parent V_2O_5 influences the density of samples more efficiently than decrease the volume due to creation of vacancies in the samples[16]. Hence, the density of samples decreases with the addition of dopant (Li_2O) in place of vanadium. On the other hand, the increase in molar volume is ascribed to the rearrangement of the lattice which leads to creating oxygen vacancies due to $VO_5 \rightarrow VO_4$ conversion with the substitution of Li^{1+} for V^{5+} (as discussed in FTIR and TGA section)[18]. This increase in molar volume supports that the Li_2O enters the network and occupy the interstitial space, which leads to an increase in free volume. Figure 2 shows the change in ionic concentration (Ni) and their inter-ionic distance (R_i) with Li_2O concentration on the cost of vanadium for all the samples. The ionic concentration increases whereas inter-ionic distance decreases (1.8–1.4 Å) with increasing Li_2O content. Decrement in the inter-ionic distance might be increased the localization effect as also confirmed by the polarization radius values (Table 1). In general, the decrease in molar volume is responsible for the decrease in inter-ionic

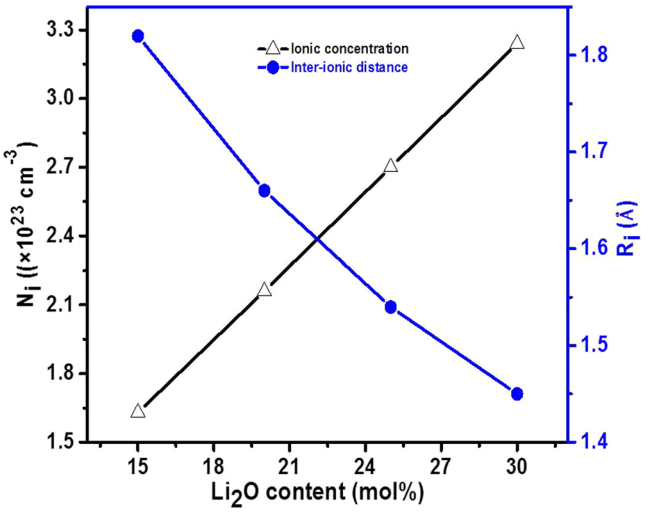

Figure 2. Change in ionic concentration and their inter-ionic distance with Li_2O content in V_2O_5.

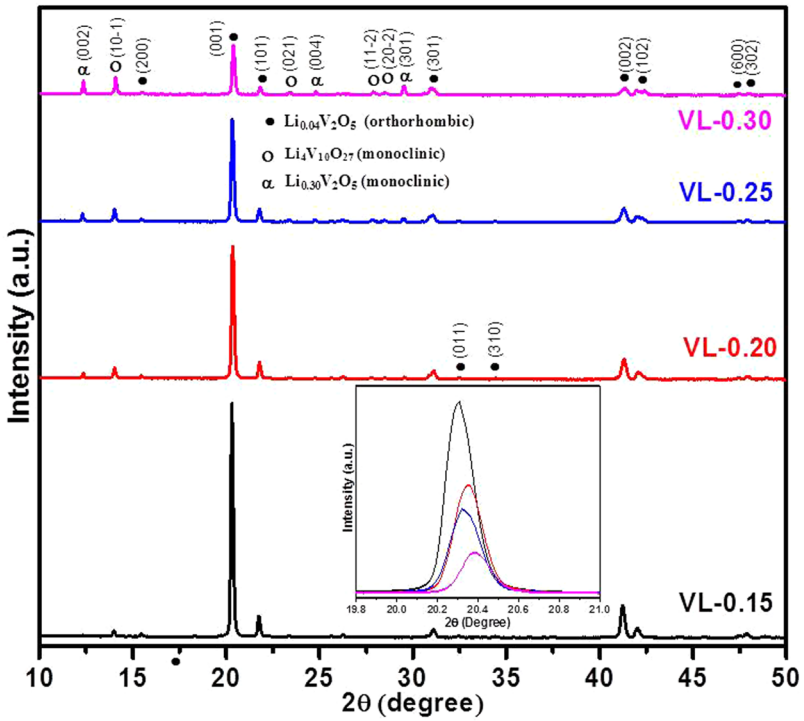

Figure 3. XRD patterns of Li_2O doped V_2O_5 as-quenched samples. The inset shows the highest intensity peak shifting towards higher diffraction angle.

distance[18]. The polaron radius (r_p) values are also calculated using R_i (Table 1). These polaron radius values decrease from 0.7 to 0.5 Å (Table 1) with Li_2O dopant due to increases R_i.The magnitude of polaron radius values suggested that they are highly localized and this localization effect increases with dopant (Li_2O) concentration.

Structural properties. *X-ray diffraction (XRD).* Figure 3 represents the XRD patterns of the Li_2O modified V_2O_5 as-quenched samples. The as-quenched samples exhibit three crystalline phases i.e. major orthorhombic $Li_{0.04}V_2O_5$ (ICDD: 01-085-0608), minor monoclinic $Li_4V_{10}O_{27}$ (ICDD: 00-046-0187) and minor monoclinic $Li_{0.30}V_2O_5$ (ICDD: 00-018-0755). The diffraction peak (001) at 20.3° corresponds to $Li_{0.04}V_2O_5$ major phase, which shows higher angle shift with Li_2O content as shown in the inset of Fig. 3. The shifting of peak towards higher diffraction angle side is the evidence of lattice contractions[19]. This is due to the smaller cationic radius Li^{1+} (0.167 nm) in comparison to V^{5+} (0.171 nm). As a result of the substitution of the larger cationic radius of V by the smaller cationic radius of Li, the lattice compression (compressive strain) arises in the $Li_{0.04}V_2O_5$ crystalline phase[19]. Further comparing the peak intensities of the phases, it is observed that the intensity of the major phase

Sample ID	E_g (eV)	E_u (eV)	σ_{ac} at 450 °C and 10^7 Hz (Scm^{-1})	σ_{dc} at 450 °C (Scm^{-1})	E_a (eV) between 50–250 °C	Present phases	Volume fraction (%)
VL-0.15	2.22	0.31	0.11	0.08	0.26	$Li_{0.04}V_2O_5$ $Li_4V_{10}O_{27}$ $Li_{0.30}V_2O_5$	95.35 3.05 1.58
VL-0.20	2.16	0.37	0.17	0.09	0.21	,,	86.45 8.30 5.10
VL-0.25	2.14	0.40	0.21	0.11	0.31	,,	80.74 11.97 7.27
VL-0.30	2.08	0.41	0.29	0.12	0.43	,,	60.26 20.70 18.00

Table 2. Optical and conductivity parameters of the as quenched samples.

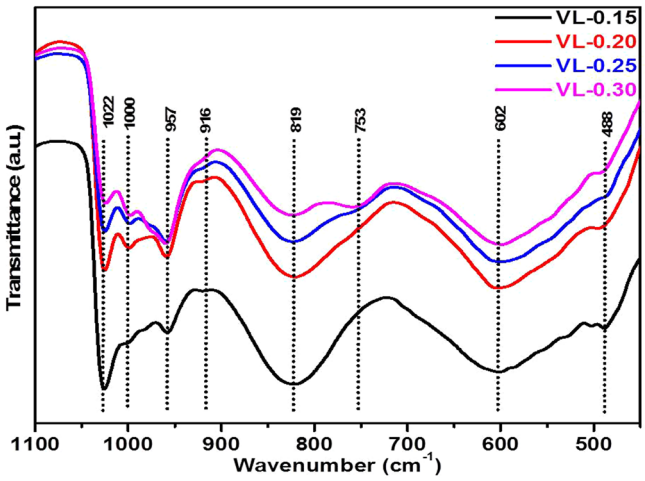

Figure 4. FTIR spectra of $V_{2-x}Li_xO_{5-\delta}$ ($0.15 \leq x \leq 0.30$) as-quenched samples.

($Li_{0.04}V_2O_5$) at 20.3° decreases whereas the intensity of the two other phases i.e. ($Li_{0.30}V_2O_5$ and $Li_4V_{10}O_{27}$) at 12.3° and 14.0° increases caused by doping of Li_2O into the V_2O_5 lattice. So, the higher concentration of Li_2O increases the volume fraction $Li_{0.30}V_2O_5$ and $Li_4V_{10}O_{27}$ phases as given in Table 2. So, the volume fraction of less symmetric phases (monoclinic) increases as dopant concentration increases.

FTIR spectroscopy analysis. Figure 4 shows infrared (IR) spectra at room temperature to investigate the structural changes with increasing concentration of Li_2O dopant. The IR spectra exhibited prominent absorption bands at 1022, 1000, 957, 916, 819, 753, 602, 488 cm^{-1}. The absorption bands at 1022 and 1000 cm^{-1} are ascribed to the vibrations of isolated V=O vanadyl groups in VO_5 trigonal bipyramids[20–22]. This characteristic stretching band with Li_2O doping present samples, which is associated with the layer structure of the V_2O_5 [20–23]. The broadness of this band decreases with increasing Li_2O content due to the decrease in the number of ionic groups and V=O bonds. Additionally, this band has a small shift to the lower wavenumber, which suggests the reduction of vanadium (V^{5+} to V^{4+}/V^{3+}) due to the addition of lithium content[24]. The V–O bond length increases due to the larger size of V^{4+} (0.67 Å) than V^{5+} (0.60 Å), results in requiring lower energy for the lattice vibration[25]. The high-temperature melt quenching of the present samples could be responsible for the reduction in the oxidation states of vanadium due to scarcity of oxygen in the furnace at high temperature[24]. The band at 957 cm^{-1} assigned to the symmetric and anti-symmetric stretching vibration of the isolated VO_2 groups in the VO_4 polyhedra[20,26]. A small kink at 916 cm^{-1} has appeared with the addition of Li_2O content. It is also assigned to the asymmetric stretching vibrations of the isolated VO_2 groups in VO_4 polyhedra[20,24]. Another band at about 819 cm^{-1} is attributed to the vibrations of isolated [VO_4] tetrahedral. The broadness of this band decreases with Li_2O content and splits into two bands (819 and 753 cm^{-1}) at maximum Li_2O content sample (VL-0.30). This new generated band is assigned to V–O–V stretching[6,20,26]. The broadening of the bands is directly related to the existence of different structural units of the same element with variable oxygens[6]. Thus, in the present case, the different structural units of vanadium decrease with the addition of Li_2O content. The band at 602 cm^{-1} is ascribed to the bending vibrations of V–O–V units. The band at 488 cm^{-1} may be assigned to the bending modes of the V_2O_5 network consisting of [VO_5] polyhedral and a characteristic vibration of Li^+ cations[20,23,27]. This band shows a small shift to the higher wavenumber with the highest doping of Li_2O (VL-0.30 sample), which shows that some portion of V^{3+}/V^{4+} oxidized to V^{5+}. The bond length between vanadium and oxygen decreases due to the smaller size of V^{5+} as compared to V^{4+}/V^{3+}, which leads to strengthening of this vibration[6,25,28]. According to Dimitriv *et al.*[26], the

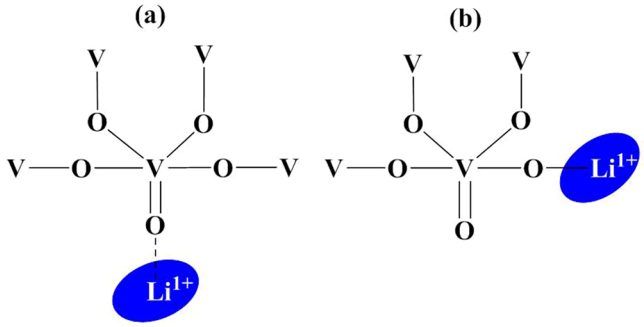

Figure 5. Schematic diagram of possible positions of the Li^{1+} ions into vanadium oxygen polyhedra: (**a**) interstitial sites; and (**b**) substitutional sites.

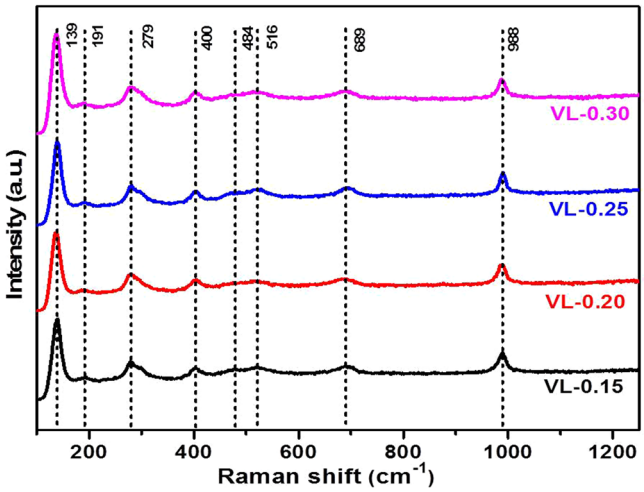

Figure 6. Raman spectra of Li_2O doped vanadium oxide as quenched samples.

vanadates can exist in the form of layers and chains and smaller complexes, which depends on the ratio of V_2O_5 and Li_2O in the samples. The Li^{1+} ions can be situated between the vanadate chains, whereas some Li ions can be form independent polyhedra (LiO_n), which can be located in the chains themselves[26]. This assumption suggests two different forms of Li ions distribution in the V–O polyhedra (interstitial sites or substitutional sites) as shown in Fig. 5(a,b). In interstitial condition, the Li ions can be located between vanadate chains and layers. Li ions can interact with the isolated V=O bonds, which leads to the longer bond length (Fig. 5(a)). In substitutional condition, Li ions can occupy positions in the vanadate chain, which leads to break the some of the weaker V-O-V bonds and form new V-O-Li bridges (Fig. 5(b))[26]. Also, there is a possibility to take place a redox reaction ($2V^{5+} + O^{2-} \rightarrow 2V^{4+} + O_2\uparrow$) during the melting of the batches at 900 °C. The V^{5+} ions take a part as a network forming positions with VO_5 structural units which can be formed V-O-Li linkages[24]. Therefore, the influence of Li ions on the V=O bond is restricted and have an indirect manifestation which leads to preserve this band at ~1022 cm^{-1} [26]. Thus, the V=O band is partially affected by Li_2O doping in the present samples.

Raman spectroscopy analysis. Raman spectra of as-quenched samples (Fig. 6) show the expected vanadia signals around 139, 191, 279, 400, 484, 516, 689 and 988 cm^{-1}. The sharp Raman band at 988 cm^{-1} is attributed to the symmetric stretching of V = O groups in pure V_2O_5 [29,30]. The intensity of this sharp V = O band increases with lithium content, establishes the formation of multilayer structures of V_2O_5 [23]. The other Raman bands around 400 and 516 cm^{-1} are attributed to the existence of the characteristic layer structure of crystalline V_2O_5. Besides these, a small shoulder at 484 cm^{-1} is also observed, which can be due to the symmetric stretching of the V-O-V bonds in V_2O_5 [29,30]. The band at 400 cm^{-1} can also be due to the Li-O stretching. Another band at 279 cm^{-1} is assigned to the deformational mode of the surface vanadyl groups. The other band around 689 cm^{-1} is due to the stretching vibration of oxygen ion in bridging position between three vanadia centers[29,30]. Finally, Raman band at 191 and 139 cm^{-1} are associated to the $[VO_5]$-$[VO_5]$ vibrations and strongly accompanying with the layered structure. They are observed at low wavenumbers due to the heavy $[VO_5]$ units[31]. Presence of all these vibrations (Figs. 4–6) substantiate the structural changes and formation of multiphase lithium vanadate in the as-quenched samples as discussed in X-ray diffraction and FTIR analysis sections.

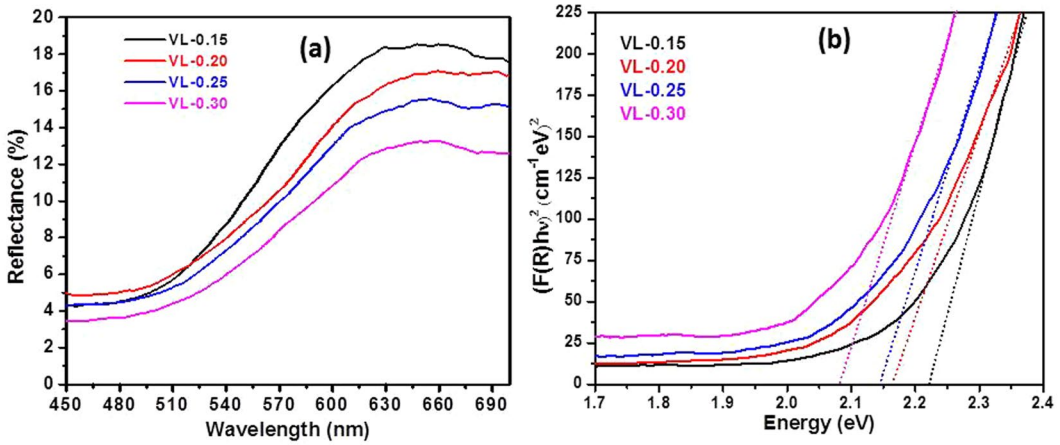

Figure 7. (**a**) The UV-vis spectra; and (**b**) the Tauc plots for $V_{2-x}Li_xO_{5-\delta}$ systems.

UV-visible spectroscopy analysis. Figure 7(a) represents the UV-visible diffused reflectance spectra (DRS) as a function of wavelength for all the samples. The reflectance for VL-0.15, VL-0.20, VL0.25 and VL-0.30 samples are 18.5%, 17%, 15.6% and 13.2%, respectively. The quenched reflectivity could be ascribed to the optical phonon confinement, which leads to the light trapping in the samples[32]. This decrement in reflectivity with increasing Li_2O dopant into V_2O_5 lattice can be due to the reflectance onset/absorption edge towards longer wavelengths (red shift). It is good agreement with other reports[32,33]. This reflectance data is used to calculate the optical band gap by Kubelka-Munk function[34].

$$F(R) = K/S = (1 - R)^2/2R \tag{1}$$

where, $F(R)$, K and S are the Kubelka-Munk function, absorption coefficient and scattering coefficient, respectively. The optical band gap is obtained from DRS using following equation.

$$(F(R)h\nu) = k(h\nu - E_g)^n \tag{2}$$

Where, k, E_g and $h\nu$ are the proportionality constant, optical band gap and incident photon energy, respectively. The exponent 'n' depends on the transition, where n = 1/2, 2, 3/2 and 3 for allowed direct, allowed indirect, forbidden direct and forbidden indirect transition, respectively[34]. The direct optical band gap of all the samples is obtained using the Tauc plot (Fig. 7(b)) by extrapolating the straight-line portion of the plots of $(F(R)h\nu)^2$ versus $h\nu$ to energy axis (x-axis) at y = 0. The Urbach energy (E_U) of the samples is calculated using the equation $\alpha(\nu) = \beta\exp(h\nu/E_U)$. The inverse of the slope of the linear portion from $lnF(R)$ versus $h\nu$ is used to measure the Urbach energy of the samples. The optical band gap decreases with increasing content of Li_2O into V_2O_5 for all the samples. The optical band gaps of the present samples are in the semiconductor range (2.22–2.08 eV) and comparable to earlier reported values by another research group[35]. The sample with the lowest concentration of Li_2O (VL-0.15) shows the highest optical band gap (2.22 eV) while the sample with the highest concentration of Li_2O (VL-0.30) shows the lowest optical band gap (2.08 eV). It indicates that the Li_2O concentration increases the defects in the present systems. The existence of variable oxidation states of vanadium as confirmed by FTIR, Raman spectroscopy and TG analysis (as discussed in next section) can be responsible for the creation of defects and oxygen vacancies in the present samples. In addition, there is a possibility to create new energy level above the valence band due to doping of Li_2O. So, the filled valence band electrons easily excited to new generated energy level by dopant led to decrease the optical band gap of the samples[36]. The Urbach energy (E_U) of the samples increases with increasing Li_2O content (Table 2). VL-0.30 sample shows the highest E_U with the lowest optical band gap signifying the presence of higher disorder as compared to other samples[34]. The optical band gap and Urbach energy both are following opposite trend to each other. It indicates that defects increase with an increase in the doping of Li_2O in place of V_2O_5.

Thermal properties. Figure 8(a) represents the DTA curves of lithium-doped V_2O_5 as-quenched samples in the temperature range of 30–800 °C. In DTA curves, all the samples exhibit three distinct endothermic peaks at a higher temperature (≥571 °C), which result from the melting points (Tm_1, Tm_2 and Tm_3) of three different phases as observed in XRD patterns. Figure 8(b) shows the TG curves of the Li_2O doped V_2O_5 as-quenched samples, which exhibit typical weight loss behavior. TGA thermograph shows a total weight loss of ~5% in the temperature range of 30–800 °C. The weight loss can be considered in three steps as marked I (30–120 °C), II (120–600 °C) and III (600–700 °C) in the TGA graph. The I step is assigned to the departure of adsorbed species and loss of water molecules[34]. The II step is associated to the reduction of V^{5+} to V^{4+}/V^{3+} ions which can be shown by the following equation[24,34].

$$2V^{5+} + O^{2-} \rightarrow 2V^{4+} + O_2\uparrow \tag{3}$$

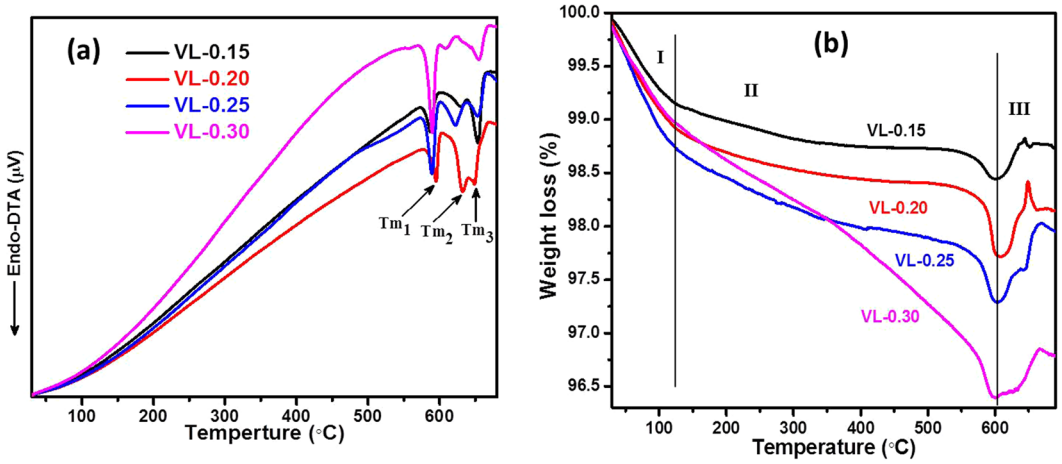

Figure 8. (**a**) DTA thermographs; and (**b**) thermal stability nature of Li_2O modified V_2O_5 systems measured at 10 °C heating rate.

In the III step, a little weight gain is observed in all the samples which can be related to the oxidation of V^{3+} to V^{5+} as written by the following equation[37,38].

$$V_2O_3 + O_2 = V_2O_5 \tag{4}$$

This weight gain during the oxidation at the higher temperature can be associated with the combination of O_2 and its vacancies in the present samples. The reduction of these systems is expected due to vanadium is believed to have a mixed valence state (V^{+3}, V^{+4} and V^{5+})[24,37,38]. It is also observed that weight loss increases with the addition of Li_2O on the cost of V_2O_5 which leads to a decrease in the thermal stability of the present samples (I and II steps). It is manifestation of waterphilic nature of the samples and it increases with an increase in Li_2O concentration. The reduction of vanadium from V^{5+} state to lower valance state is also increases with the addition of Li_2O content. The chemical stability also decreases with Li_2O concentration which is also manifested by Urbach energy and FTIR analysis of the samples. All the samples exhibit good thermal and chemical stability in the temperature range of ~300–550 °C without any phase transition (Fig. 8(a,b)) except VL-0.30 sample. However, sample with the lowest content of Li_2O (7.5 mol%, VL0-0.15) shows the highest thermal and chemical stability in the temperature range of ~300–550 °C in comparison to other samples. Therefore, these samples can be used as electrolytes for solid oxide fuel cells or batteries applications.

Conducting studies. It is a well-known fact that hopping mechanism and band conduction are responsible for the electrical conduction in these types of materials[6,39]. The frequency dependent conductivity, σ_{ac} of the samples is determined using the following relation[6,39].

$$\sigma_{ac}(\omega) = \varepsilon_0\omega'' = 2\pi f\varepsilon' tan\delta \tag{5}$$

where, ε_0 ε', ε'', f and $tan\delta$ are the permittivity of free space (8.854×10^{-12} Fm^{-1}), dielectric constant, dielectric loss, frequency (in Hz) of the applied electric field and tangent of loss, respectively. Figure 9(a–d) illustrates the AC conductivity (σ_{ac}) variation with frequency and temperatures (50–450 °C, step size of 50 °C). The conductivity is almost frequency independent at low frequency region (plateau region) and corresponds to the DC conductivity (σ_{dc}) of the samples[40]. At the same time, the conductivity is dependent on frequency (σ_{ac}) at higher frequency region (dispersion region) and increases with increasing frequency[6,15,39,40]. The plateau region signifies the randomness of ionic diffusion which is due to the long-range order transport and appreciable diffusion of mobile ions in response to the applied ac field while the dispersion region signifies the conductivity relaxation phenomena in present samples[6,7,15,40,41]. It is also observed that σ_{ac} increases with increasing temperature (50–450 °C) for all the samples which supports the semiconductor nature of the samples[6,42]. Generally, the conductivity in such type of materials depends on the concentration and mobility of mobile ions/charge carriers i.e. electrons and holes[6,42]. The mobility of mobile ions/charge carriers increases with increasing temperature which leads to increasing overall conductivity as observed in the present samples. It can be understood by the fact that thermal energy (temperature) excites more electrons from valence band to conduction band resulting in higher conductivity. Further, according to the Jonscher's universal power law, σ_{ac} can be written as[6,41,43,44]:

$$\sigma_{ac}(\omega, T) = \sigma_{dc}(T) + A\omega^s \tag{6}$$

where, A is the temperature dependent constant of the material, ω is the angular frequency and s is the frequency and temperature dependent exponent that lies between 0–1. DC conductivity ($\sigma_{dc}(T)$) is calculated to extrapolate AC conductivity at the lowest frequency (Fig. 9) and given in Table 2. The activation energy (E_a) of the conduction is calculated using the Arrhenius plot (Fig. 10) between $ln\sigma_{dc}$ and reciprocal of temperature ($1000/T$) by the following equation.

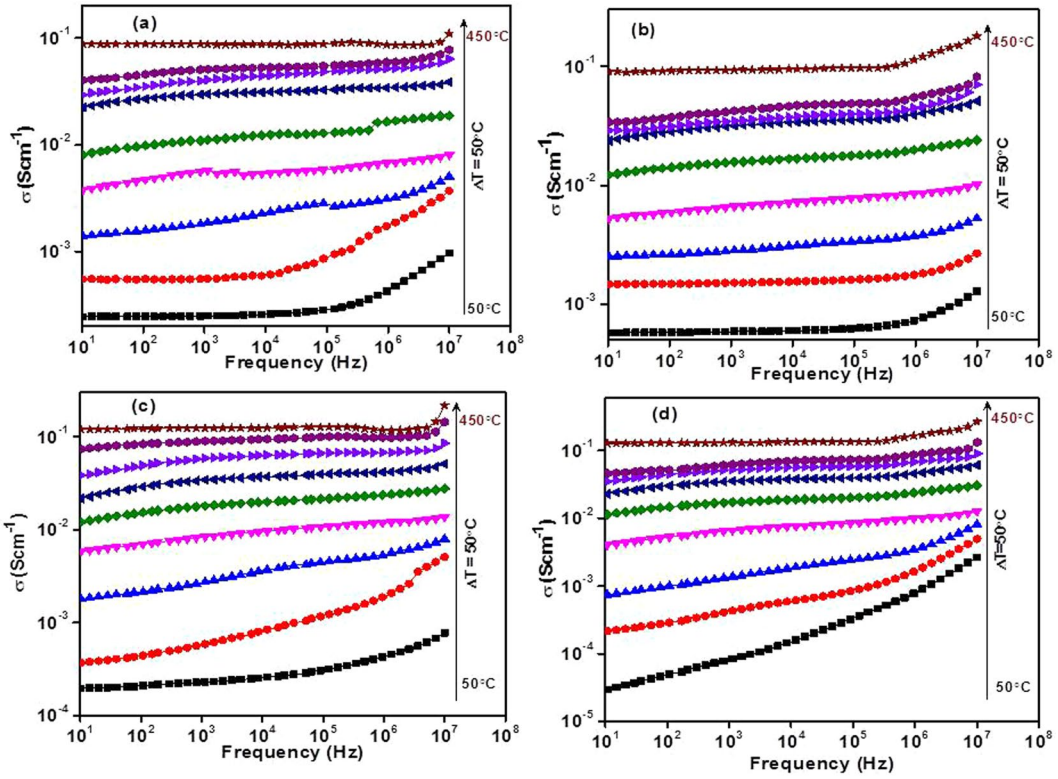

Figure 9. Change in conductivity as a function of frequency and temperatures for (**a**) VL-0.15 (**b**) VL-0.20 (**c**) VL-0.25 (**d**) VL-0.30 samples.

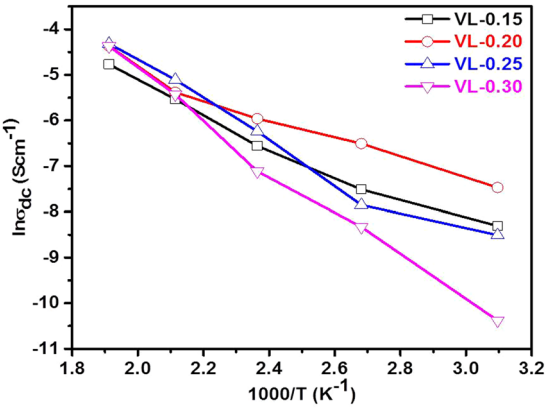

Figure 10. Change in dc conductivity as a function of the reciprocal temperature of VL-0.15 to VL-0.30 samples.

$$\sigma_{dc} = \sigma_o \exp(-E_a/k_B T) \quad (7)$$

where, σ_o and k_B are the pre-exponential factor, and Boltzmann's constant, respectively. The values of σ_{ac} and σ_{dc} show an increasing trend with an increase in lithium content (7.5–15 mol%) as shown in Fig. 11. AC conductivity lies in the range of 0.11–0.29 Scm^{-1} at 450 °C and 10^7 Hz whereas DC conductivity lies in the range of 0.08–0.12 Scm^{-1} at 450 °C. In vanadate materials, conductivity depends on the small polarons hopping (SPH) between V^{4+} site to the neighboring V^{5+} site[6,7,39]. SPH directly affects by the mobility and number of mobile charge carriers. On the replacement of V^{5+} by Li^+, structure of the systems becomes more open due to transition from VO_4 tetrahedral to VO_5 trigonal bipyramid as discussed in physical parameters and structural properties. This structural change is responsible for a significant increase in oxygen vacancies with an increase in hopping of ions which leads to an increase in conductivity[4,5,42]. In addition, decrement in density, inter-ionic distance, polaron radius and optical band gap of the samples also support this increasing trend of conductivity with the addition of Li_2O

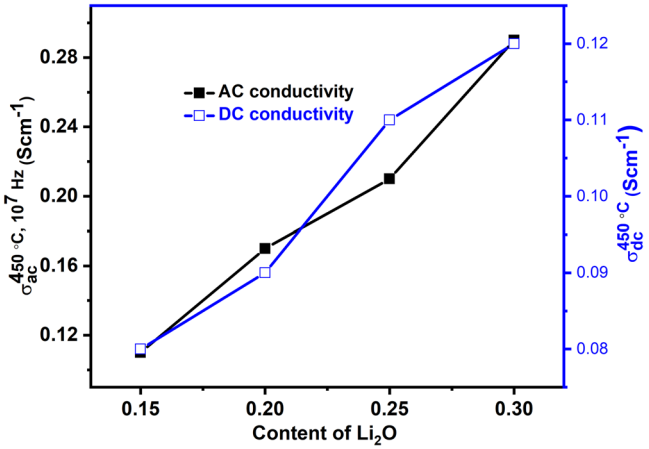

Figure 11. Change in AC and DC conductivity with Li_2O content in V_2O_5 for all samples.

on the cost of V_2O_5[7]. The calculated activation energy values of dc conduction are depicted in Table 2. The activation energy increases with increasing content of Li_2O except VL-0.20 sample and lies in the range of 0.26–0.43 eV (Table 2). These activation energy values clearly suggest that the ionic conduction increases with Li_2O concentration into V_2O_5 in the present samples.

Conclusion

The influence of Li_2O addition on physical parameters, structural, optical, thermal and conducting properties of $V_{2-x}Li_xO_{5-\delta}$ ($0.15 \leq x \leq 0.30$) systems have been investigated. XRD patterns confirmed the presence of three crystalline phases. The presence of mixed valence states of vanadium is confirmed by spectroscopic investigations. The optical band gap is decreased with Li_2O concentration. Thermal stability is found to decrease with the Li_2O addition in place of V_2O_5. AC and DC conductivity are found to enhance by the addition of Li_2O due to the creation of more hoping sites. Sample with the highest content of Li_2O (15 mol%, VL-0.30) exhibited the highest DC conductivity i.e. 0.12 Scm^{-1} at 450 °C. It is observed that the transport mechanism in lithium vanadate systems is attributed to small polaron hopping (SPH) between V^{4+} to V^{5+} states, which is increased by the addition of lithium into vanadium. The present samples exhibit good DC and AC conductivity. Therefore, these materials can be considered as electrolytes for batteries/solid oxide fuel cells applications.

Materials and Methods

Powder of V_2O_5 (Loba, Chemie, 99% purity) and Li_2O (Sigma Aldrich, 97% purity) were used as raw materials to prepare compositions of $V_{2-x}Li_xO_{5-\delta}$, where x = 0.15(VL-15), x = 0.20(VL-20), x = 0.25(VL-25) and x = 0.30(VL-30) via melt and quench technique. The prescribed compositions are mixed using agate mortar and pestle in acetone medium for 2 h. The mixed batches were melted at 900 °C in recrystallized aluminum crucibles in an electric furnace followed by copper plates quenching in the air. The standard Archimedes principle is used to measure density (D) at room temperature of as-quenched samples with xylene as immersion liquid (0.863 gcm^{-3}). The molar volume (V_m) of as-quenched samples was calculated using the following equation,

$$V_m = \sum_i M_i/\rho \tag{8}$$

where, ρ and M_i are the density and molar mass of the samples, respectively. The concentration of Li ions (N) was calculated by $N_i = N_A \times mol\%\ of\ cation \times valency/V_m$, where N_A and M is the Avogadro's number and molecular weight, respectively. The average inter-ionic distance (R_i) was calculated using $R_i = (1/N)^{1/3}$. The polaron radius was calculated by $r_p = (R_i/2) \times (\pi/6)^{1/3}$. The X-ray diffraction (XRD) patterns of crushed samples were recorded by PANalytical X'Perts Pro MPD diffractometer with Cu-Kα radiations (λ = 1.54 Å). The scan rate and scan range were 2°min^{-1} and 10–80°, respectively. Fourier transform infra-red (FTIR) spectra of as-quenched samples were recorded in the wavenumber range of 200–4000 cm^{-1} at room temperature using Perkin Elmer-Spectrum-RF-1 FTIR spectrometer. The finely ground powder of as-quenched sample and KBr powder are mixed together to palletized for the FTIR measurement. The Raman spectra of the powder samples were recorded over the spectral range of 100–5000 cm^{-1} using Features STR 500 Airix Raman system equipped with Ar laser (532 nm) as the excitation source.

A double beam UV-Vis spectrophotometer (Model: Hitachi 3900H) was used to record diffused reflectance spectra (DRS) at room temperature between the wavelength 200–800 nm. Thermal analysis was carried out using TG/DTA (Exstar TG/DTA 6300) instrument of as-quenched powder samples in N_2 medium with a heating rate of 10 °C/min over the range of room temperature to 1000 °C. The dielectric and conductivity analysis carried out using SI-1260 Solartron analytical LCR impedance analyzer. Both sides of the as-quenched samples are coated with Pt using 3000-FC auto fine coater from JEOL to serve as an electrode. The variation in impedance with frequency and temperature were studied from 10Hz-1MHz and 50–400 °C, respectively.

Received: 16 April 2019; Accepted: 15 November 2019;
Published online: 23 January 2020

References

1. Yang, Z. *et al*. A short review of cathode poisoning and corrosion in solid oxide fuel cell. *Int. J. Hydrogen Energ.* **42**, 24948–24959 (2017).
2. Wanga, J. *et al*. Effect of humidity on $La_{0.4}Sr_{0.6}Co_{0.2}Fe_{0.7}Nb_{0.1}O_{3-\delta}$ cathode of solid oxide fuel cells. *Int. J. Hydrogen Energ.* **44**, 3055–3062 (2019).
3. Mahato, N., Banerjee, A., Gupta, A., Omar, S. & Balani, K. Progress in material selection for solid oxide fuel cell technology: A review. *Prog. Mat. Sci.* **72**, 141–337 (2015).
4. Kant, R., Singh, K. & Pandey, O. P. Synthesis and characterization of bismuth vanadate electrolyte material with aluminium doping for SOFC application. *Int. J. Hydrogen Energ.* **33**, 455–462 (2008).
5. Gupta, S. & Singh, K. γ-Phase stabilized $Bi_4Ba_xV_{2-x}O_{11-\delta}$ ($0.0 \leq x \leq 0.20$): Structural, thermal and conducting properties. *Solid State Ionics* **278**, 233–238 (2015).
6. Khan, S. & Singh, K. Effect of MgO on structural, thermal and conducting properties of $V_{2-X}Mg_XO_{5-\delta}$($x = 0.05-0.30$) systems. *Ceram. Int.* **45**, 695–701 (2019).
7. Al-Hajry, A., Al-Shahrani, A. & El-Desoky, M. M. Structural and other physical properties of barium vanadate glasses. *Mater. Chem. Phys.* **95**, 300–306 (2006).
8. Afyon, S., Krumeich, F., Mensing, C., Borgschulte, A. & Nesper, R. New High Capacity Cathode Materials for Rechargeable Li-ion Batteries: Vanadate-Borate Glasses. *Sci. Rep*. **4**, 7113 (1–7) (2014).
9. Vannier, R. N. *et al*. $Bi_4V_2O_{11}$ polymorph crystal structures related to their electrical properties. *Solid State Ionics* **157**, 147–153 (2003).
10. Abrahams, I. *et al*. Effects of preparation parameters on oxygen stoichiometry in $Bi_4V_2O_{11-\delta}$. *J. Mater. Chem.* **8**, 1213–1217 (1998).
11. Punia, R. *et al*. Effect of Bi_2O_3 on structural, optical, and other physical properties of semiconducting zinc vanadate glasses. *J. Appl. Phys.* **110**, 33527–33533 (2011).
12. Abrahams, I. & Krok, F. A model for the mechanism of low temperature ionic conduction in divalent-substituted γ-BIMEVOXes. *Solid State Ionics* **157**, 139–145 (2003).
13. Chakrabarty, D. K., Guha, D. & Biswas, A. B. Electrical properties of vanadium pentoxide doped with lithium and sodium in the α-phase range. *J. Mater. Sci.* **11**, 1347–1353 (1976).
14. Punia, R., Kundu, R. S., Dult, M., Murugavel, S. & Kishore, N. Temperature and frequency dependent conductivity of bismuth zinc vanadate semiconducting glassy system. *J. Appl. Phys.* **112**, 83701–83705 (2012).
15. Khoon, T. F., Hassan, J., Wahab, Z. A. & Azis, R. S. Electrical conductivity and dielectric studies of MnO_2 doped V_2O_5. *Results Phys.* **6**, 420–427 (2016).
16. Tsuzuki, A., Kani, K., Watari, K. & Torii, Y. Properties of the glasses prepared by rapid quenching in the V_2O_5-MO(M = Mg, Ca and Ba) system. *J. Mater. Sci.* **28**, 4063–4067 (1993).
17. Abrahams, I., Krok, F., Malys, M. & Bush, A. J. Defect structure and ionic conductivity as a function of thermal history in BIMGVOX solid electrolytes. *J. Mater. Sci.* **36**, 1099–1104 (2001).
18. Moustafa, M. G. & Hassaan, M. Y. Optical and dielectric properties of transparent ZrO_2-TiO_2-$Li_2B_4O_7$ glass system. *J. Alloy. Compd.* **710**, 312–322 (2017).
19. Shirage, P. M. *et al*. Sr- and Ni-doping in ZnO nanorods synthesized by a simple wet chemical method as excellent materials for CO and CO_2 gas sensing. *RSC Adv.* **6**, 82733–82742 (2016).
20. Jeyalakshmi, K., Vijayakumar, S., Nagamuthu, S. & Muralidharan, G. Effect of annealing temperature on the supercapacitor behaviour of β-V_2O_5 thin films. *Mater. Res. Bull.* **48**, 760–766 (2013).
21. Mandal, S. & Ghosh, A. Structure and physical properties of glassy lead vanadates. *Phys. Rev. B* **48**, 9388–9393 (1993).
22. Rao, L. S., Reddy, M. S., Reddy, M. R. & Veeraiah, N. Dielectric dispersion in Li_2O-MoO_3-B_2O_3 glass system doped with V_2O_5. *J. Alloy. Compd.* **464**, 472–482 (2008).
23. Iordanova, R., Dimitriev, Y., Dimitrov, V. & Klissurski, D. Structure of V_2O_5-MoO_3-Fe_2O_3 glasses. *J. Non-Cryst. Solids* **167**, 74–80 (1994).
24. Ibrahim, S., Marzouk, M. A. & Komy, G. M. E. Structural Characteristics and Electrical Conductivity of Vanadium-doped lithium Ultra phosphate Glasses. *Silicon* **9**, 403–410 (2017).
25. Vijayakumar, M., Selvasekarapandian, S., Kesavamoorthy, R., Nakamura, K. & Kanashiro, T. Vibrational and impedance spectroscopic studies on lithium vanadate prepared by solid-state reaction. *Mat. Lett.* **57**, 3618–3622 (2003).
26. Dimitriev, Y., Dimitrov, V., Arnaudov, M. & Topalov, D. IR-Spectral Study of Vanadate Vitreous Systems. *J. Non-Cryst. Solids* **57**, 147-156-957 (1983).
27. Padmaja, G. & Kistaiah, P. Infrared and Raman Spectroscopic Studies on Alkali Borate Glasses: Evidence of Mixed Alkali Effect. *J. Phys. Chem. A* **113**, 2397–2404 (2009).
28. Zhou, X. *et al*. Carbon black anchored vanadium oxide nanobelts and their post-sintering counterpart (V_2O_5 nanobelts) as high performance cathode materials for lithium ion batteries. *Phys. Chem. Chem. Phys.* **16**, 3973–3982 (2014).
29. Lee, S. *et al*. Raman spectroscopic studies of amorphous vanadium oxide thin films. *Solid State Ionics* **165**, 111–116 (2003).
30. Sethi, D. *et al*. Photocatalytic destruction of Escherichia coli in water by V_2O_5/TiO_2. *J. Photoch. Photobio. B* **144**, 68–74 (2015).
31. Zhan, S. *et al*. Effects of Cr doping on the structural and electrochemical properties of V_2O_5. *J. Alloy. Compd.* **479**, 652–656 (2009).
32. Ghosh, A. *et al*. Study of faceted Au nanoparticle capped ZnO nanowires: antireflection, surface enhanced Raman spectroscopy and photoluminescence aspects. *J. Phys. D: Appl. Phys.* **48**, 055303–055313 (2015).
33. Lee, S. H. Jr., Duty, G. E. J. & Xu J, C. E. Light confinement-induced antireflection of ZnO nanocones. *Appl. Phys. Lett.* **99**, 153113–153116 (2011).
34. Khan, S., Kaur, G. & Singh, K. Effect of ZrO_2 on dielectric, optical and structural properties of yttrium calcium borosilicate glasses. *Ceram. Int.* **43**, 722–727 (2017).
35. Kumar, S. K. & Menon, C. S. Optical and electrical properties of vanadium pentoxide thin films. *phys. stat. sol. (a)* **153**, 439–444 (1996).
36. Kumari, J. C. S., Nishanthi, S. T., Dhanalakshmi, J., Ahila, M. & Padiyan, D. P. Bio-active synthesis of tin oxide nanoparticles using eggshell membrane for energy storage application. *Appl. Surf. Sci.* **441**, 530–537 (2018).
37. Hui, S. & Petric, A. Conductivity and stability of $SrVO_3$ and mixed perovskites at low oxygen partial pressures. *Solid State Ionics* **143**, 275–283 (2001).
38. Cheng, Z., Zha, S., Aguilar, L. & Liu, M. Chemical, electrical, and thermal properties of strontium doped lanthanum vanadate. *Solid State Ionics* **176**, 1921–1928 (2005).
39. Yadav, A. *et al*. Electrical characterization of lithium bismuth borate glasses containing cobalt/vanadium ions. *Solid State Ionics* **312**, 21–31 (2017).
40. Thakur, S., Pandey, O. P. & Singh, K. structural and dielectric properties of $Bi(1-x)Sr_xMnO_3$ ($0.40 \leq x \leq 0.55$). *Ceram. Int.* **39**, 6165–6174 (2013).

41. Tashtousha, N., Qudaha, A. M. & El-Desoky, M. M. Compositional dependence of the electrical conductivity of calcium vanadate glassy semiconductors. *J. Phys. Chem. Solids* **68**, 1926–1932 (2007).
42. Dutta, A., Sinha, T. P., Jena, P. & Adak, S. Ac conductivity and dielectric relaxation in ionically conducting soda-lime-silicate glasses. *J. Non-Cryst. Solids* **354**, 3952–3957 (2008).
43. Kaur, N., Kaur, G., Khan, S. & Singh, K. Conductivity, dielectric, and structural studies of (30-x) SrO-xBaO-10Al_2O_3-45SiO_2-5B_2O_3-10Y_2O_3 ($5 \leq x \leq 25$) glasses. *Ionics* **24**, 2343–2353 (2017).
44. Jaidka, S., Khan, S. & Singh, K. Na_2O doped CeO_2 and their structural, optical, conducting and dielectric properties. *Physica B* **550**, 189–198 (2018).

Acknowledgements
The authors are also thankful to IIT, Bombay for providing impedance analyzer characterization. One of the authors (Savidh Khan) thanks Km. Abida, SCBC, TIET, Patiala for her help to carry out the work. One of the authors (Savidh Khan) also thankful to CSIR under the Letter No. 09/677(0037)/2019-EMR-I for providing the financial assistance as direct-SRF.

Author contributions
S. Khan carried out the majority of the presented work synthesis, characterizations and analysis of the lithium doped vanadium. The present study was conceptualized and supervised by K. Singh., Professor, Thapar Institute of Engineering and Technology, Patiala, India.

Competing interests
The authors declare no competing interests.

Additional information
Correspondence and requests for materials should be addressed to K.S.

Reprints and permissions information is available at www.nature.com/reprints.

Publisher's note Springer Nature remains neutral with regard to jurisdictional claims in published maps and institutional affiliations.